Global distribution of near-surface hydrogen on Mars

W. C. Feldman,[1] T. H. Prettyman,[1] S. Maurice,[2] J. J. Plaut,[3] D. L. Bish,[1] D. T. Vaniman,[1] M. T. Mellon,[4] A. E. Metzger,[3] S. W. Squyres,[5] S. Karunatillake,[5] W. V. Boynton,[6] R. C. Elphic,[1] H. O. Funsten,[1] D. J. Lawrence,[1] and R. L. Tokar[1]

Received 18 July 2003; revised 1 July 2004; accepted 4 August 2004; published 22 September 2004.

[1] Neutron data observed using the Neutron Spectrometer aboard 2001 Mars Odyssey provide a lower limit to the global inventory of Martian water-equivalent hydrogen. Hydrogen-rich deposits ranging between about 20% and 100% water-equivalent by mass are found poleward of ±50° latitude, and less rich, but significant, deposits are found at near-equatorial latitudes. The equatorial deposits between ±45° latitude range between 2% and 10% water-equivalent hydrogen by mass and reach their maximum in two regions that straddle the 0-km elevation contour. Higher water abundances, up to ~11%, are required in subsurface regolith of some equatorial regions if the upper 10 g/cm^2 of regolith is desiccated, as suggested on average by comparison of epithermal and fast neutron data. The hydrogen contents of surface soils in the latitude range between 50° and 80° north and south are equal within data uncertainties. A lower-limit estimate of the global inventory of near surface hydrogen amounts to a global water layer about 14 cm thick if the reservoir sampled from orbit is assumed to be 1 m thick. *INDEX TERMS:* 5410 Planetology: Solid Surface Planets: Composition; 5416 Planetology: Solid Surface Planets: Glaciation; 5462 Planetology: Solid Surface Planets: Polar regions; 6225 Planetology: Solar System Objects: Mars; *KEYWORDS:* composition, glaciation, Mars

Citation: Feldman, W. C., et al. (2004), Global distribution of near-surface hydrogen on Mars, *J. Geophys. Res.*, *109*, E09006, doi:10.1029/2003JE002160.

1. Introduction

[2] Prime objectives of the Neutron Spectrometer (NS) component of the Gamma-Ray Spectrometer suite of instruments aboard 2001 Mars Odyssey are to identify the major reservoirs of hydrogen on Mars, determine their relative contributions to the total water inventory, and estimate that portion of the current inventory that is near the surface. Measurements of epithermal and fast neutron currents can provide a lower limit to hydrogen abundances in the uppermost meter of Mars.

[3] Observations from the Viking orbiters and landers positively identified two of these reservoirs: the polar deposits and the atmosphere. By far the largest is in the polar residual water-ice caps and their surrounding layered deposits, which are thought to contain sufficient water to cover Mars with a global-equivalent layer (GEL) about 30 m deep [*Carr*, 1986; *Smith et al.*, 1999]. The second is contained in the atmosphere, which if deposited on the surface, would cover Mars with a thin film of water about 10^{-5} m thick [*Jakosky and Farmer*, 1982]. Although negligible in comparison, the fact that an atmospheric reservoir exists shows that it can provide a conduit that links transient reservoirs of near-surface water molecules [*Jakosky and Haberle*, 1992; *Mellon and Jakosky*, 1993].

[4] It has long been speculated that Mars has had, and may still retain, a far larger reservoir of water. Geomorphic features such as rampart craters, collapsed chaotic terrain, massive outflow channels, and valley networks provide strong support for the past existence of large quantities of surface and near-surface water [*Squyres*, 1989; *Baker*, 2001; *Carr*, 1986, 1996; *Jakosky and Phillips*, 2001]. Analysis of geomorphic features with probable aqueous origins led to an estimate of a total water inventory equivalent to a GEL between 100 and 500 m thick [*Carr*, 1986]. Measurements of the D/H ratio suggest that between 5 and 50 m of this inventory has been lost to space [*Yung et al.*, 1988; *Luhman et al.*, 1992; *Carr*, 1990; *Jakosky*, 1991; *Leshin*, 2000]. Altogether, these estimates lead to between 50 and 495 m of unaccounted water from the ancient Martian inventory.

[5] First analyses of Mars Odyssey neutron and gamma-ray data showed that large reservoirs of hydrogen do indeed exist in the uppermost meter of Martian soils poleward of about ±50° latitude [*Boynton et al.*, 2002; *Feldman et al.*, 2002b; *Mitrofanov et al.*, 2002; *Tokar et al.*, 2002]. Mars Odyssey neutron observations also revealed a near equatorial hydrogen reservoir [*Feldman et al.*, 2002b].

[6] Quantitative estimates of hydrogen abundances in these investigations were originally normalized to an as-

[1]Los Alamos National Laboratory, Los Alamos, New Mexico, USA.
[2]Observatoire Midi-Pyrenees, Toulouse, France.
[3]Jet Propulsion Laboratory, Pasadena, California, USA.
[4]Laboratory for Atmospheric and Space Physics, University of Colorado, Boulder, Colorado, USA.
[5]Center for Radiophysics and Space Research, Cornell University, Ithaca, New York, USA.
[6]Department of Planetary Sciences, University of Arizona, Tucson, Arizona, USA.

0148-0227/04/2003JE002160$09.00

sumed 1% H_2O content by mass for the Viking 1 landing site [*Biemann et al.*, 1977; *Anderson and Tice*, 1979]. However, a recent analysis of the seasonal variation of the CO_2 frost cover at both poles has allowed an independent absolute calibration of the three neutron energy bands measured using the Mars Odyssey NS [*Feldman et al.*, 2003; *Prettyman et al.*, 2004]. This calibration now allows a reinterpretation of neutron fluxes measured globally to provide a lower limit to the hydrogen abundance within about 1 m of the Martian surface. We note that although neutron spectroscopy as applied here is sensitive only to the abundance of hydrogen regardless of its molecular associations, we will quantify our measurements throughout this paper in terms of water-equivalent hydrogen (WEH) mass fraction (or just plain H_2O mass fraction) in order to conform to common usage in the current literature. Hopefully this should not be misleading.

[7] Even though our newly calibrated results are more accurate, a more complete determination of H_2O requires knowledge of the stratigraphy and spatial heterogeneity of H_2O-bearing layers. The presence of an overlying relatively desiccated layer can mask enhanced abundances within lower layers [*Feldman et al.*, 1993, 2003], and heterogeneity of H_2O abundances within the NS field of view appears as a nonlinear average abundance. Hence the interpretations presented here generally provide lower limits to H_2O abundances in the major H_2O-bearing layers within the uppermost meter of Mars. However, there are places on Mars, such as the high-latitude northern terrain surrounding the residual water-ice cap near the north pole, that are so spatially heterogeneous, multilayered in depth near the surface, and topographically variable (thereby leading to large spatial variations in atmospheric thickness) that errors in interpreting the measured neutron counting rates in terms of water-equivalent-hydrogen can lead to large, and at present, unquantifiable uncertainties.

2. CO_2 Frost-Free Epithermal and Fast Neutron Counting Rates

[8] The sensor element of the NS is a segmented block of borated plastic scintillator [*Feldman et al.*, 2002a; *Boynton et al.*, 2004]. This design allows measurements of upward currents of thermal (energies, E, less than 0.4 eV), epithermal (0.4 eV < E < 0.7 MeV) and fast (0.7 < E < 1.6 MeV) neutrons. Absolute calibration of all three energy ranges was made using counting rates measured when the spacecraft was poleward of ±85° latitude. The calibration at latitudes >+85° was made during a time interval centered at an areocentric longitude, $L_S = 10°$ [*Feldman et al.*, 2003], when the northern seasonal CO_2 frost cap was near its maximum. This calibration consisted of equating the thermal, epithermal, and fast counting rates measured poleward of +85° to those predicted by simulations using Monte Carlo Neutral Particle computer code, MCNPX, fitted with a special planetary boundary patch developed for Mars [*Prettyman et al.*, 2004], coupled to a model of the instrument response function (determined from calibrations in the laboratory before launch [*Feldman et al.*, 2002a]). The model of the seasonal CO_2 frost cover at maximum used as input the thickness determined from measurements of the attenuation of hydrogen 2.223 MeV capture gamma-rays. The calibration at latitudes <−85° was made near $L_s = 150°$, when the southern seasonal CO_2 frost cap was likewise near its maximum [*Prettyman et al.*, 2004].

[9] CO_2 frost-free maps of thermal, epithermal, and fast neutron counting rates constructed from data measured between 19 Feb. 2002 and 20 April, 2003 are shown in Figure 1. The procedure used to remove data that were contaminated by seasonal deposits of CO_2 frost was to separate the total data set into three parts. Those data measured before the autumnal equinox in the south (corresponding to an areocentric longitude of $L_s = 0°$) were used to generate the portion of the data set poleward of a longitudinal-dependent southern boundary given by the dashed white line in Figure 1. This boundary was determined from a break in the magnitude of RMS variations of epithermal neutron counting rates constructed using the entire data set. Spatial locations on Mars having a high RMS variation were judged to be subject to seasonal variations in the CO_2 frost cover that is apparent in the epithermal-neutron counting rates. A similar procedure for the northern boundary used data measured after $L_s = 100°$. Data within the middle band of latitudes were averaged over the entire data set. Correction of all counting rates for variations in cosmic ray flux, global variations in atmospheric thickness, and effects of variations in the NS high voltage were made by normalizing peak areas for each measured neutron energy spectrum, to the average counts summed over ±0.5 day when the spacecraft was equatorward of ±30° latitude [*Prettyman et al.*, 2004]. Corrections were also made for variations in atmospheric thickness due to topography by normalizing all measurements made within 45° of the equator to what should be expected for the neutron currents at the top of a 16 g/cm^2 thick atmosphere [*Prettyman et al.*, 2003b]. No such corrections were made poleward of ±45° latitude.

[10] An overview of Figure 1 shows that Mars can be separated into three spatial domains that have very different character. The first domain north of about +50° latitude is marked by very low thermal, epithermal, and fast neutron counting rates. The minimum rate surrounds the north pole and a secondary minimum is centered at about −125° longitude (a positive east-longitude convention is used here) between +65° and +75° latitude. This domain of low counting rates is pinched off, being narrowest at about −45° longitude just north of Acidalia in the Vastitas Borealis formation. In the second spatial domain south of about −50° latitude, the maps are also dominated by low counting rates in a broad ellipse with its long axis centered on about +100° longitude. In the third spatial domain at near-equatorial latitudes between ±50°, a mixed pattern of both low and high counting rates exists, having relative minima along the equator near Arabia Terra between about 0° to +50° longitude, and along −10° latitude, crossing the 180° longitude meridian.

3. Derivation of H_2O Mass Fractions From Counting Rates and Their Uncertainties

[11] The connection between measured neutron counting rates and neutron energy distributions was made by combining our absolute calibration with simulations of counting rates using MCNPX. These simulations assumed a three-

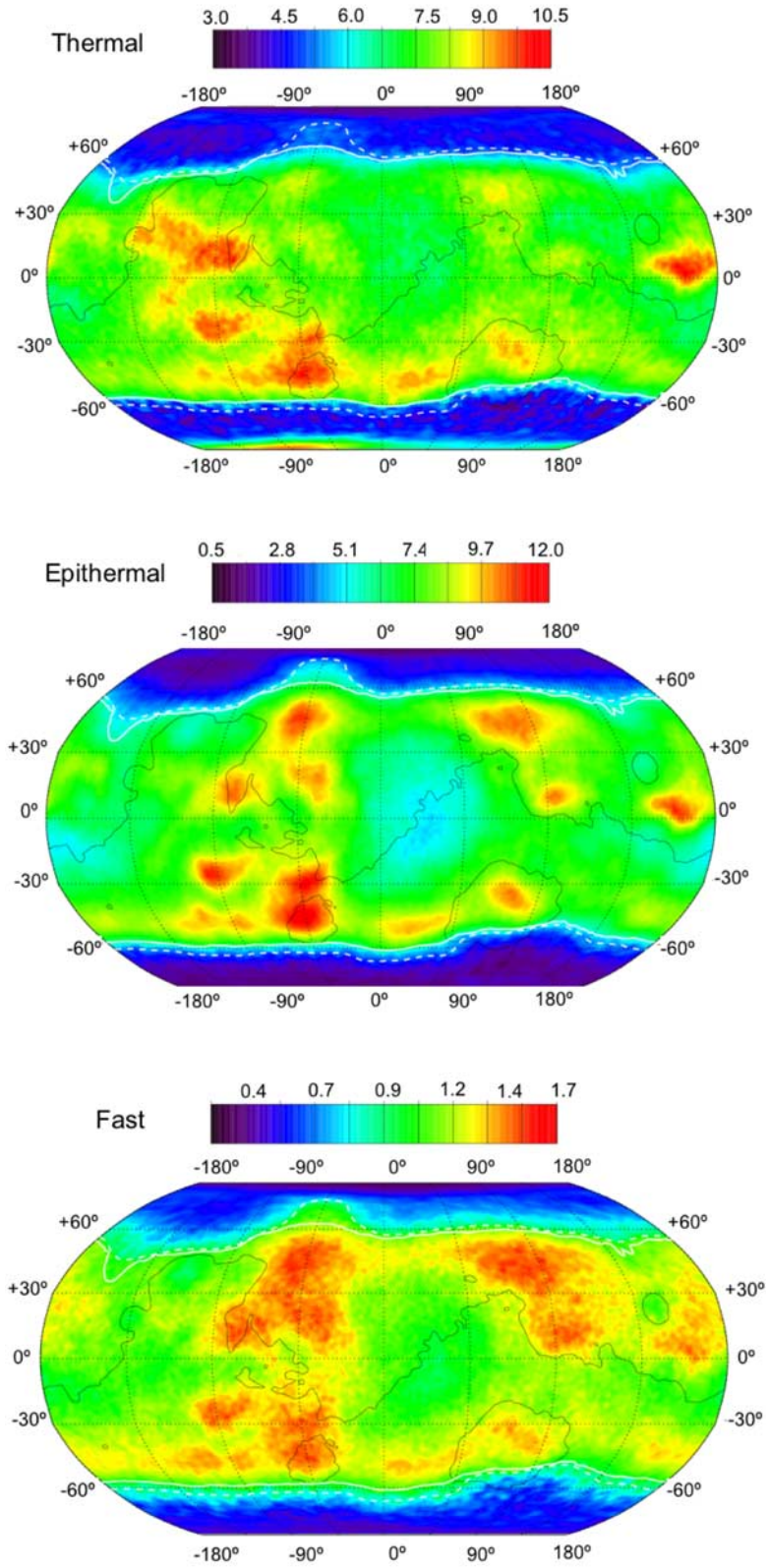

Figure 1. Thermal, epithermal, and fast neutron CO_2 frost-free maps of Mars. Data north of the northern white dashed wavy line were measured after the northern summer solstice ($100° < L_s < 151°$), and data south of the southern dashed wavy line were measured during the late summer in the south ($329° < L_s < 1.7°$). The 0-km elevation contour (black line) is shown for reference. The solid white lines separate the poleward regions having water abundances larger than about 11% by mass from those at near equatorial latitudes that have abundances that are less than 11%.

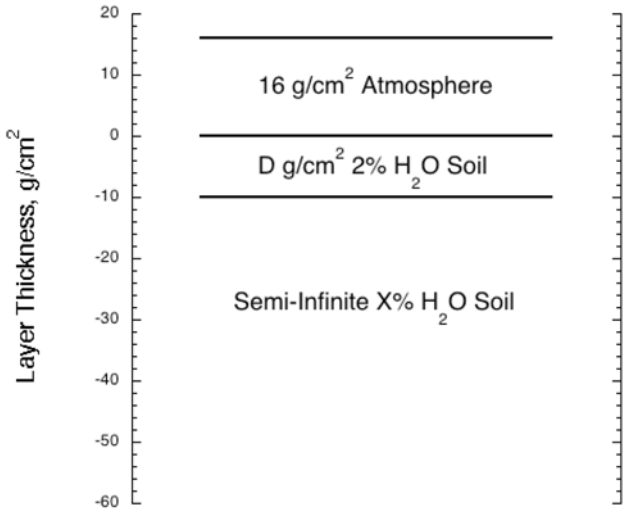

Figure 2. A simple model of the stratigraphy of water-equivalent hydrogen deposits near the surface of Mars.

layered model of the Martian surface and atmosphere as shown in Figure 2. Three parameters were varied in these simulations: the thickness of the atmosphere, in g/cm^2, the thickness of the uppermost layer of soil, D, assumed to contain 2% H_2O by mass, in g/cm^2, and the mass percent of H_2O in a semi-infinite lower layer, X. The composition of the atmosphere was assumed to be that measured by *Owen et al.* [1977], and the composition of the soil was that measured at Mars Pathfinder [*Wänke et al.*, 2001]. Normalization of all our measurements to a 16 g/cm^2 atmosphere as just mentioned, thereby reduces the number of free parameters in the model in Figure 2 from three to two, D and X, respectively.

[12] The relationship between the mass fraction of water-equivalent hydrogen (M_{H2O}) of soil and the calibrated epithermal neutron [Epi] and fast neutron [Fast] counting rates (given by the variable Z), can be fit quite well by the product of polynomial and power law functions,

$$M_{H2O} = [B\ Z^p] \Sigma\ A_i\ Z^i, \quad (1)$$

for $0.02 < M_{H2O} < 1.0$, and $0 \leq i \leq 5$. The parameters of equation (1) are given in Table 1, and an overlay of both functions and the simulated counting rates for a range of M_{H2O} values between 0.02 and 1.0, are shown in Figure 3. The fits are seen to be excellent.

[13] The parameters for both epithermal and fast neutrons in equation (1) correspond to a 16 g/cm^2 atmosphere and no dry upper soil layer of 2% H_2O (D = 0). Similar simulations using a wide range of surface compositions have shown that the relationship given by equation (1) for epithermal neutrons is minimally sensitive to the host soil composition [*Feldman et al.*, 1993; *Prettyman et al.*, 2003a]. However, it does depend on both the abundance of water and its gradient with depth, which according to the model illustrated in Figure 2, corresponds to variable thicknesses, D, of a 2% H_2O layer. Enhanced abundances of H_2O buried beneath layers having lower H_2O abundance will generally appear from orbit as having some intermediate abundance that depends on D.

Table 1. Parameters for Equation (1)

Parameter	Epithermal Neutrons	Fast Neutrons
Z	[Epi]	[Fast]
B	1.061	0.07535
p	−1.567	−2.476
A_0	0.6991	0.96
A_1	0.3291	−0.8696
A_2	−0.1152	+3.034
A_3	0.01986	−2.553
A_4	−0.001651	0.5917
A_5	5.12×10^{-5}	0

[14] For fast neutrons, equation (1) will change somewhat for other soil compositions because the fast neutron flux varies linearly with the average atomic weight, $\langle A \rangle$, of surface soils [*Maurice et al.*, 2000; *Gasnault et al.*, 2001]. Nevertheless, this variation should be less than that detected on the Moon (which amounted to ±15% full-width at full maximum, FWFM) because in dust-covered areas, aeolian processes are expected to homogenize the composition of Fe and Ti, which are the dominant contributors to $\langle A \rangle$. Where the dust cover is light, the abundance of Ti is generally low and that of Fe does not appear to vary much [*Bandfield et al.*, 2000]. Although the abundance of Cl may be variable on Mars, it should not affect $\langle A \rangle$ because its abundance is thought to be generally lower than about 1% [*Wänke et al.*, 2001; *Foley et al.*, 2003]. However, we caution that if these expectations are not met in reality, then interpretations of measured fast neutron currents are subject to possible ±15% relative errors in counting rates. Subsequent errors on other dependent parameters derived from these counting rates may then be likewise higher.

[15] The uncertainties in H_2O abundances derived from analyses of epithermal and fast neutron currents have

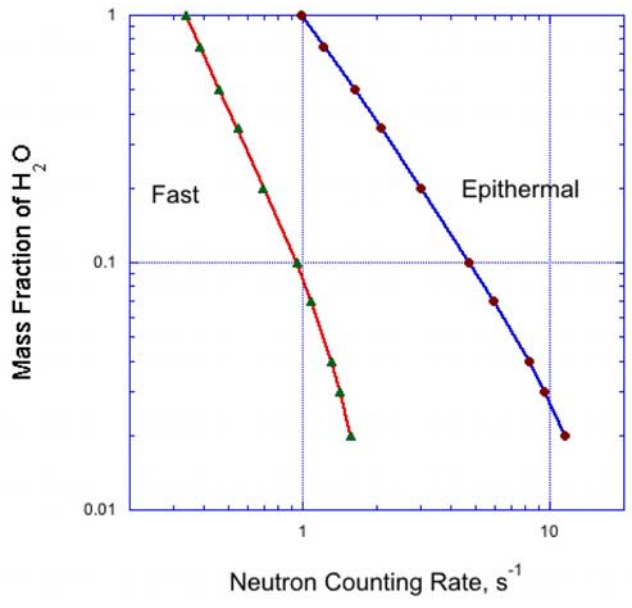

Figure 3. The correlation between mass fraction of H_2O and epithermal and fast neutron counting rates simulated for an assumed semi-infinite soil stratigraphy having the base composition measured at the Pathfinder landing site.

several contributions. These include (1) statistical uncertainties in the average counting rate due to the random nature of counting experiments; (2) systematic errors in the data reduction algorithm; (3) uncertainties in the calibration constants; and (4) uncertainties in models of the Martian surface and atmosphere. We address each of these in turn:

[16] 1. The counting rates used to carry out our analysis of water abundance are averages over 19.75 s measurement intervals. The standard deviation of these averages for selected regions is given by the population standard deviation divided by the square root of the number of observations [*Bevington and Robinson*, 1992]. The uncertainty depends on the number of samples and the counting rate. In the north, the standard deviation in the mean summertime epithermal counting rate poleward of +85° was determined to be less than 1% from measurements made over a 4.5 month period. Away from the pole, at +60°, the standard deviation was about 2.5% for a 5° equal angle pixel. In the south, the standard deviation in the mean summertime epithermal counting rate poleward of −85° was about 1% and a typical 5° equal angle pixel at −60° was 6.5%. The uncertainty is lower in the north due to the fact that only a portion of the southern summer was observed during mapping to date. In comparison, the uncertainty for a 5° equal area pixel at the equator is 1%.

[17] 2. Systematic errors in the data reduction algorithm include errors in determining the peak area, mostly introduced by fluctuations in the gain of the spectrometer, uncertainties introduced by the cosmic ray normalization algorithm, errors in our atmospheric correction algorithm, and uncertainties in determining the background counting rate. We assumed the background counting rate resulting from cosmic ray interactions with spacecraft material to be zero for epithermal neutrons because it was measured during cruise to be insignificant [*Feldman et al.*, 2002a]. Errors in peak area determination apply to epithermal neutrons only, and are expected to be largest at high latitudes where the counting rate is near the background (far from the conditions encountered during calibration).

[18] 3. The calibration constant may contain a systematic error due to the assumption that the CO_2 frost during northern winter is uniform in thickness over the footprint of the spectrometer for data acquired poleward of +85°. In addition, the thickness of the frost used to calibrate the spectrometer was determined from measurements of the attenuation of the hydrogen 2.223 MeV capture gamma ray. An effective attenuation coefficient for this analysis was determined using a Monte Carlo radiation transport model, which can also introduce systematic errors due to the use of various assumptions, including the cosmic ray input energy and angle distribution, the intranuclear cascade model (which produces the primary high energy neutrons), and cross section data sets used to model neutron transport. By carrying out a variational analysis on the input parameters for the Monte Carlo model, we conclude that the uncertainty in the footprint-averaged frost thickness based on gamma-ray attenuation is less than ±5%.

[19] 4. To determine minimum water abundance, we assumed that the surface consists of a single, semi-infinite layer. We then contrasted the minimum water abundance as determined by epithermal and fast neutrons. Differences encountered between ±45° latitude were explained (as will be described later) by a model in which the average soil consists of two layers, a dry upper layer covering a relatively hydrogen-rich lower layer that is close enough to the surface to be sensed by the spectrometer. We have applied this model only to latitudes equatorward of ±45° in this study because the heterogeneity and stratigraphy of water ice at more polar latitudes may be considerably more complicated than that pictured in Figure 2 [*Farmer and Doms*, 1979; *Paige*, 1992; *Mellon and Jakosky*, 1993]. In our analysis, we assumed that the non-hydrogen composition of the surface is that of Pathfinder soil. This assumption could affect the interpretation of the fast neutrons, and hence our estimate of depth, as previously mentioned. Other more complex physical models of the surface are possible and perhaps likely, but cannot be fit with the two observable parameters used in this study. Finally, the counting rate of the surface physical models is determined using a Monte Carlo radiation transport calculation combined with the spectrometer response function, both of which can be in error.

[20] Our attempt to estimate, correct for, and thereby control systematic effects associated with the reduction of data is an ongoing process of continuous improvement. At present, we believe that our total relative uncertainty in deriving counting rates from raw epithermal neutron data binned into 5° × 5° quasi-equal-area spatial elements is less than about ±10%. We find that the uncertainty in the calibration constants amounts to about ±5% for epithermal neutrons [*Feldman et al.*, 2003] and <±10% for fast neutrons [*Prettyman et al.*, 2004]. An exploration of variations in input parameters used for MCNPX shows that relative uncertainties in translating measured counting rates in 5° × 5° quasi-equal area surface elements equatorward of ±82.5° amounts to less than about 7% on average. If the foregoing contributions to uncertainties are folded together in quadrature, the result leads us to expect that our estimates of H_2O mass fractions from epithermal neutron counting rates are accurate to less than about ±15% relative uncertainty.

[21] Of course, these uncertainties are in addition to those caused by the fact that our results are non-unique. We are interpreting two measured quantities (epithermal and fast neutron counting rates) to determine the concentration of H_2O near the Martian surface, which in reality, requires more than two parameters to describe. In addition to the hydrogen concentration as a function of depth, we also need to know the elemental composition as a function of depth and the heterogeneity of all variables over the 300 km radius FWHM spatial footprint of the Mars Odyssey Neutron Spectrometer. In terms of our simple model illustrated in Figure 2, we therefore need to determine the H_2O mass fraction of both the top and bottom layers, the thickness of the top layer, and the composition of a possible two-layer model (for example, to account for the presence of a duricrust layer) whose boundary may not necessarily coincide with the boundary of the two-layered H_2O abundance model.

[22] In summary, because of the excellent counting statistics of neutron data, we believe that the relative hydrogen abundances that we have found are a robust result. Absolute abundances, however, are harder to determine, and we recognize that there could be some difficult-to-quantify uncertainties in absolute abundances due to systematic effects. One approach to estimating such systematic effects would be to examine our derived H_2O abundance for an ice-

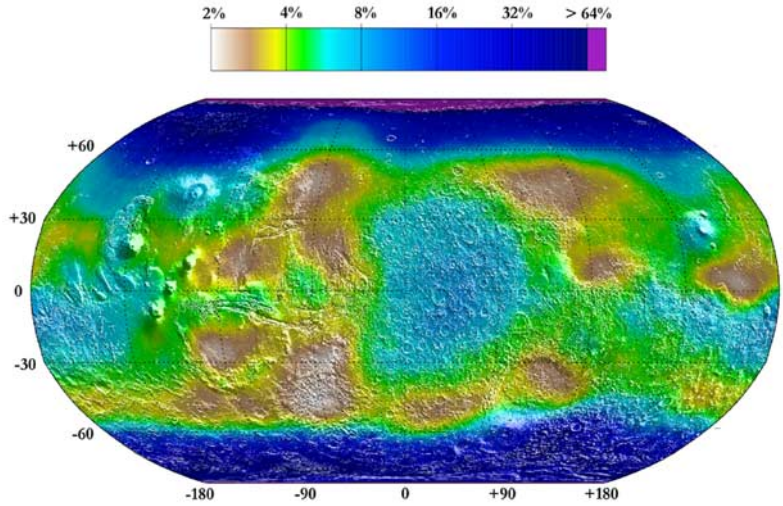

Figure 4. A Robinson projection of the water-equivalent hydrogen content of the semi-infinite layer of water-bearing soils derived from epithermal-neutron counting rates.

rich locale like the northern residual H_2O cap. The minimum counting rates of epithermal and fast neutrons observed within 300 km radius spatial elements poleward of 82.5° latitude are 0.97 ± 0.1 and 0.44 ± 0.06 cps, respectively, which yield a WEH of 103 ± 16% and 58 ± 22% when entered into equation (1). The size of the residual cap, however, is smaller than the footprint of the NS, and allowance needs to be made for the surrounding terrain in the footprint. We have attempted some simple modeling of the influence of this terrain, and the result has been WEH values substantially lower than those quoted above. This discrepancy could result from shortcomings in our model, of course, but it also could be indicative of unrecognized systematic effects in equation (1). We leave the resolution of this apparent discrepancy to future work. And while these uncertainties encourage us to be cautious in the interpretation of our derived absolute H_2O abundances, we retain a high confidence in the spatial variability in near-surface H_2O on Mars that we have found.

4. Maps of Lower-Limit Estimates of Hydrogen on Mars

[23] The epithermal-neutron counting-rate map in the middle panel of Figure 1 was converted to lower-limit abundances of water-equivalent hydrogen using equation (1). We expect this conversion will yield water abundances that are less than what may exist deeper below the surface. According to the model stratigraphy shown in Figure 2, our derived abundances then only approximate that of the lower semi-infinite soil layer. The surface dust cover (which in our model corresponds to the uppermost 2% H_2O-bearing layer) will be subject to larger temperature variations in response to diurnal and seasonal variations in solar insolation, and should therefore be less able to retain its water inventory [*Leighton and Murray*, 1966; *Farmer and Doms*, 1979; *Mellon and Jakosky*, 1993]. A Robinson projection of the resultant water-equivalent hydrogen map is shown in Figure 4. The color scale was chosen to be logarithmic to provide adequate resolution of the large range in H_2O abundance encountered over the planet. A shaded relief map of Martian topography from data measured using the Mars Orbiter Laser Altimeter (MOLA) [*Smith et al.*, 1999] is superimposed to allow a cross reference between the various water-abundance and surface terrain features.

[24] Inspection of Figure 4 shows that the two largest discrete reservoirs of hydrogen-rich soils near the equator occur at approximately antipodal longitudes. That in the neighborhood of Arabia Terra is centered near the equator at +25° longitude, and the other is just below the equator at about +185° longitude. These reservoirs have longitudinal extension that appear to follow the 0-km contour line (shown later in Figure 9) for a considerable longitudinal distance before they connect to northerly directed hydrogen-rich lanes that follow the western slopes of Olympus, Arsia, and Pavonis Mons in the west, and through the center of Elysium Mons in the east. Northeast of the hydrogen rich lane that skirts the western edge of Tharsis is a relative maximum that is centered on Alba Patera.

[25] We note also from Figure 4 that the lowest apparent abundance of water-equivalent hydrogen is 2% by mass. This result was used to set the water-equivalent hydrogen abundance in the uppermost, relatively desiccated layer in Figure 2 at 2% by mass. In this case the two-layer model reduces to one semi-infinite layer.

[26] Orthographic north and south polar projections poleward of ±50° latitude of the epithermal-neutron H_2O maps are shown in the top panels of Figures 5 and 6, respectively. Because the data volume used for both polar domains was less than that available for the near-equatorial domain (due to selection of a reduced high-latitude data subset to eliminate seasonal CO_2 frost contamination), both high-latitude maps were smoothed using a 4° arc-radius circular box-car filter. The global map in Figure 4 was similarly smoothed for consistency. The bottom panels of both Figures 5 and 6 overlay maps of the Martian topography measured using MOLA [*Smith et al.*, 1999] with contours of constant water-equivalent hydrogen mass fraction. The outermost contour in both figures corresponds to 10% H_2O by mass, and successive poleward contours correspond to 20%, 30%, 40%, 50%, and 60% mass fractions. Inspection of the top panel of Figure 5 shows that H_2O abundances

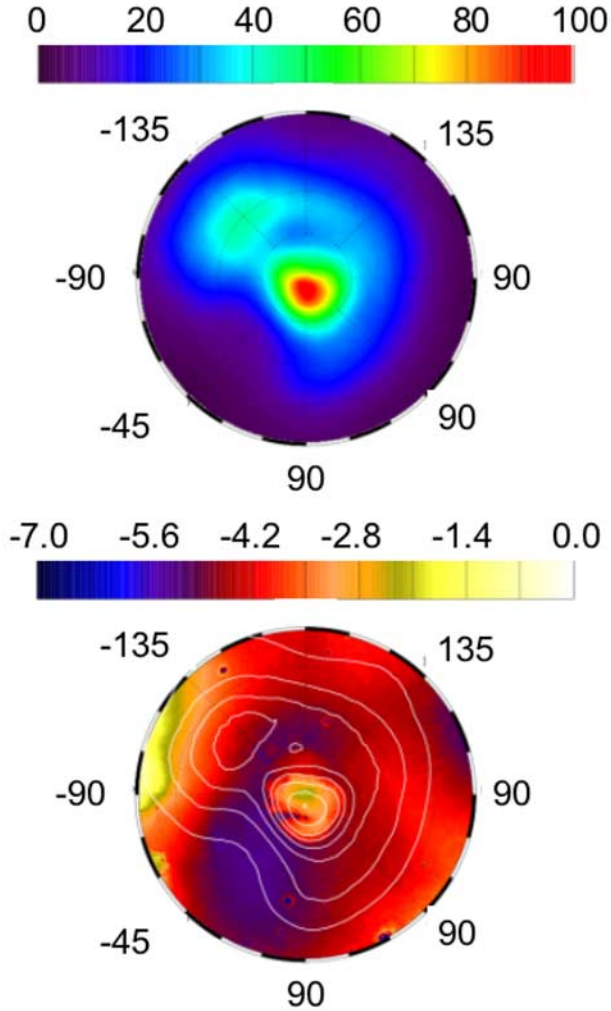

Figure 5. Orthographic projection of lower-limit abundances of water-equivalent hydrogen at latitudes poleward of +50°. Dashed circles correspond to latitudes of 60°, 70°, and 80°. Contours of water abundance corresponding to 10% (outermost contour), 20%, 30%, 40%, 50%, 60%, 80%, and 100% (inner contour) by mass are overlaid on a MOLA map of topography in orthographic projection in the bottom panel.

around the north pole range up to about 100 ± 16% by mass, while those in the south range between 20% and about 50% by mass (as shown in Figure 6). Apparent abundances of H_2O equatorward of these contours (the third reservoir) range between about 2% and 10% by mass as shown in Figure 4, with an average value of about 5%.

5. Stratigraphy of H_2O Mass Fraction Equatorward of ±45° Latitude

[27] A first-order approximation to the depth of burial of the major H_2O-containing layer can be determined through a combined study of epithermal- and fast-neutron counting rates. As mentioned previously, conversion of both counting-rate maps in Figure 1 to H_2O using equation (1), yields lower limits. However, the fast-neutron limit is expected to be lower than the epithermal limit because the fast signature of hydrogen drops off more rapidly with depth. This fact is demonstrated in Figure 7. Input to the MCNPX simulation given by the uppermost straight line is for a 16 g/cm^2 atmosphere and no upper layer of 2% H_2O soil. The slope of this line is unity and its intercept is zero so that the apparent mass fraction of H_2O through applications of equation (1) is equal to that of the semi-infinite water-bearing layer. The next two curves show the relationship between the apparent and actual mass fraction of H_2O of a semi-infinite water-bearing layer that is buried beneath a 10 g/cm^2 2% H_2O layer. Note that the prediction of H_2O mass fraction from fast neutrons is less than that from epithermal neutrons. Both curves meet at 2% H_2O mass fraction because at that point, there exists only a single semi-infinite layer. The lowest two curves are from simulations of a 20 g/cm^2 uppermost 2% H_2O layer. Note that

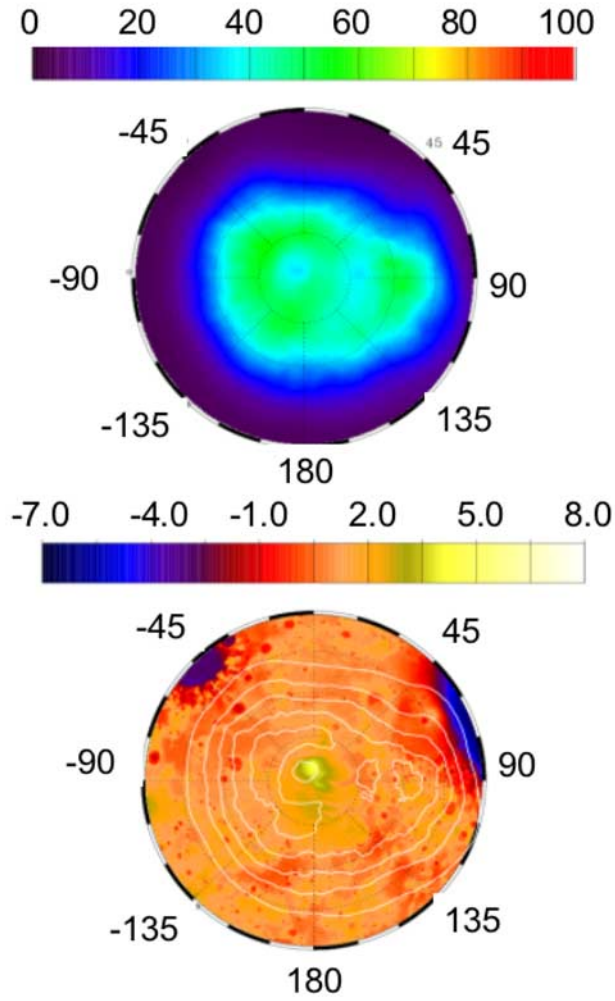

Figure 6. Orthographic projection of lower-limit abundances of water-equivalent hydrogen at latitudes poleward of −50°. Dashed circles correspond to latitudes of 60°, 70°, and 80°. Contours of water abundance corresponding to 10%, 20%, 30%, 40%, and 50% by mass are overlaid on a MOLA map of topography in orthographic projection in the bottom panel.

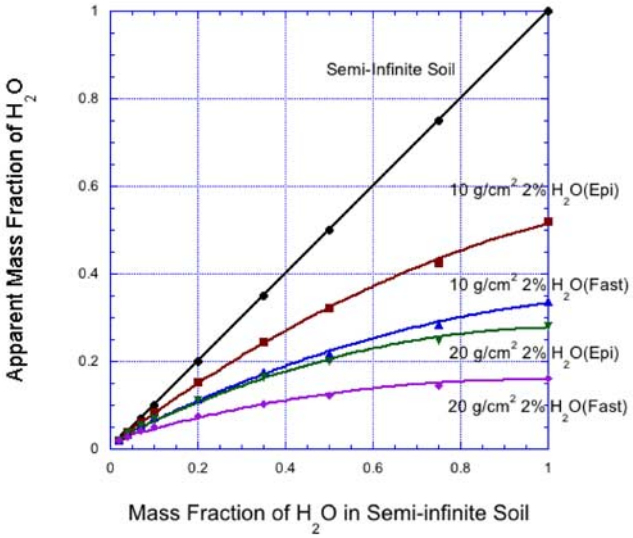

Figure 7. The relationship between apparent mass fractions (using equation (1)) and the actual mass fractions of H_2O in the lower semi-infinite layer simulated using MCNPX for the stratigraphy model illustrated in Figure 2.

predictions of the apparent H_2O mass fractions for both epithermal and fast neutrons are reduced further while maintaining a higher H_2O mass fraction from epithermal neutrons. As the thickness of the uppermost desiccated layer gets larger than about 100 g/cm^2, both curves flatten out to a constant prediction of 2% H_2O. In other words, a water-rich soil layer buried beneath a relatively desiccated layer can no longer be detected from orbit through measurements of escaping neutrons if its physical thickness is larger than about one meter.

[28] The results shown in Figure 7 are summarized in Figure 8 in a form that will be used later in our analysis.

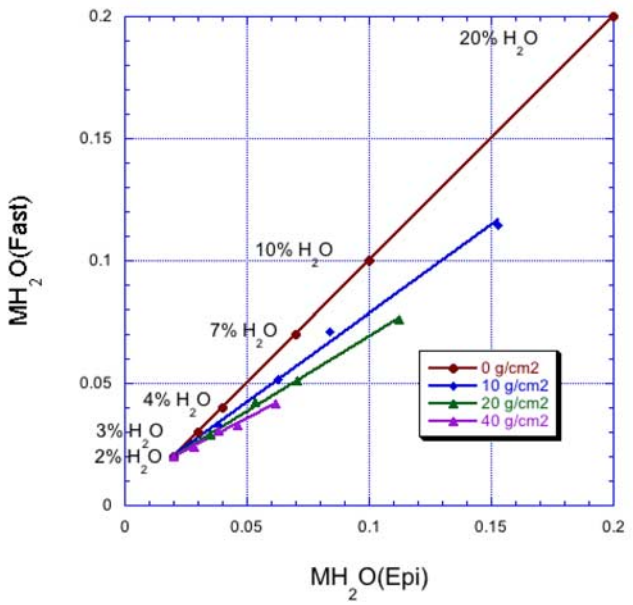

Figure 8. The relationship between mass fractions of H_2O determined from measured fast and epithermal neutron-counting rates using the stratigraphy model in Figure 2.

Table 2. Parameters for the Equation $M_{H2O}(Fast) = A_o + A_1 M_{H2O}(Epi)$ for Various Thicknesses of an Assumed 2% H_2O Overburden

Thickness of 2% H_2O Layer	A_o	A_1
0 g/cm^2	0.0	1.0
10 g/cm^2	0.00615	0.7208
20 g/cm^2	0.00805	0.6094
40 g/cm^2	0.00939	0.5276

Here we plot the relationship between the apparent mass fraction of H_2O from measured fast neutron currents to that determined from measured epithermal neutrons. The uppermost straight line with unit slope and zero intercept corresponds to no uppermost 2% H_2O layer. The next three lines are for 10, 20, and 40 g/cm^2 2% H_2O layers. These lines apply only for H_2O in the lower layer that is less than 20% by mass. Their $M_{H2O}(Epi) = 0$ intercepts, A_o, and slopes, A_1, are given in Table 2. Note that the slopes decrease monotonically with increasing thickness of the uppermost layer, that all lines cross over at a percentage mass fraction of 2% H_2O, and the apparent percentage mass fractions for a given water content of the semi-infinite layer decrease monotonically with increasing thickness. Although not shown here, at thicknesses greater than about 40 g/cm^2 of 2% H_2O, the slopes remain constant.

[29] Maps of the percentage mass fractions of H_2O constructed from epithermal and fast neutron counting

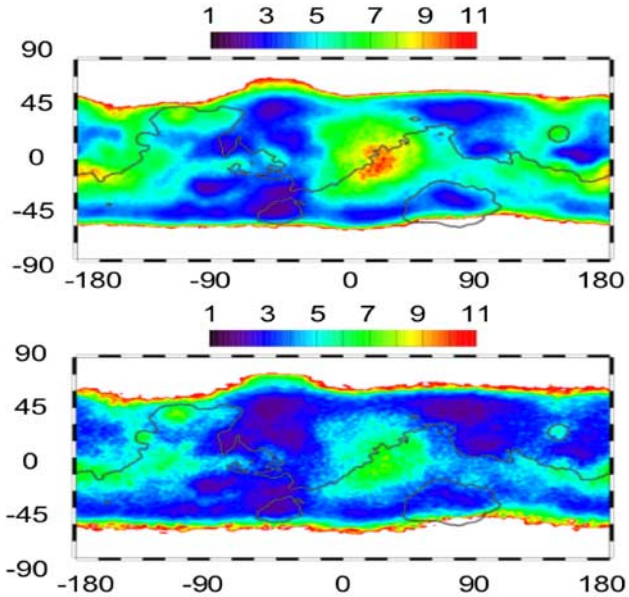

Figure 9. Lower-limit estimates of the water abundance on Mars. The map in the top panel is derived from epithermal neutron counting rates using equation (1) with parameters from the epithermal-neutron column in Table 1, and that in the bottom panel is derived from fast neutron counting rates using equation (1) with parameters from the fast-neutron column in Table 1. Both maps are in cylindrical projection. The elevation contour at 0 km is superimposed on both maps. Regions poleward of the wavy red lines have water-equivalent hydrogen abundances larger than 11%.

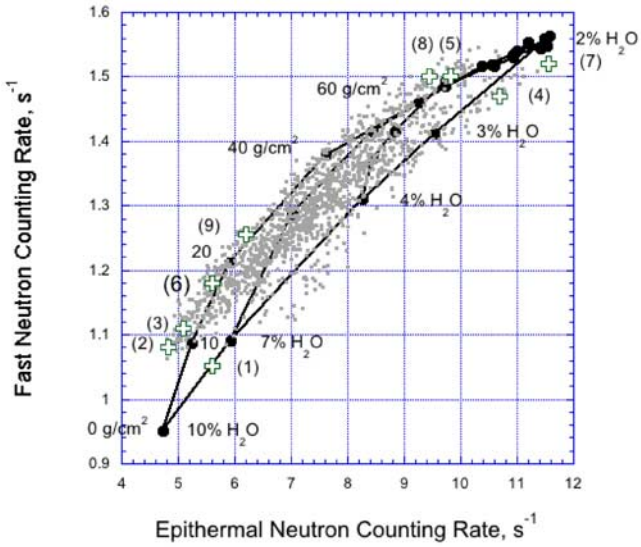

Figure 10. Measured fast and epithermal neutron counting rates within quasi equal-area spatial elements equivalent to 5° × 5° latitude by longitude squares at the equator. These data are overlaid by MCNPX simulations of counting rates under the assumption of a single, semi-infinite soil layer having Pathfinder composition modeled with varying mass fractions of water-equivalent hydrogen (given by the bottom right-hand arc). Also superimposed are Pathfinder composition simulations that correspond to the burial of a relatively water-rich layer beneath a relatively desiccated layer containing 2% H_2O (given by the three arcs at the top left). Measured counting rates for the selection of nine midlatitude sites listed in Table 3 are included.

rates are shown in the top and bottom panels of Figure 9, respectively. Three different reservoirs are evident. The components having H_2O abundances larger than 11% by mass poleward of ±45° latitude correspond to terrain poleward of the red wavy contours in both panels. This contour was smoothed and included in the counting-rate maps of Figure 1 as solid white lines. The 0-km contour of constant elevation as measured by MOLA (solid black and white line) is also drawn in Figure 9.

[30] In order to provide quantitative context for the information contained in Figure 9, measured counting rates equatorward of ±45° were binned into 5° latitude quasi-equal area spatial elements. The longitudinal widths of each spatial element at a given latitude are adjusted such that there are an integral number in each 360° circle, but each has a width such that their areas are close to that for a 5° latitude by 5° longitude square element at the equator. Although a preliminary analysis of many MCNPX simulations shows that thermal neutrons should be more sensitive to burial depth than are fast neutrons, we are purposely avoiding them at this point because a unique interpretation of thermal neutrons requires knowledge of the composition of surface soils (specifically, the abundances of the strongest neutron absorbers, Fe, Ti, Cl, Gd, and Sm). These abundances are not presently available from Mars Odyssey gamma-ray observations. Scatterplots of 5° × 5° fast-neutron and epithermal-neutron counting rates are shown in Figure 10. Inspection shows a strong correlation. The linear regression is

$$[\text{Fast}] = 0.074[\text{Epi}] + 0.75, \quad (2)$$

with a correlation coefficient of R = 0.92.

[31] Superimposed on the measurements in Figure 10 are simulations of counting rates for a semi-infinite soil having the Pathfinder composition and variable H_2O weight percent (the lower-most arc that is labeled with% H_2O). Three different two-layer models having variable thickness (in g/cm^2) of 2% H_2O above 10%, 7%, and 4% H_2O semi-infinite soils (the three uppermost arcs that connect 10%, 7%, and 4% H_2O with 2% H_2O), respectively, are also shown. Inspection shows that most of the measured fast- and epithermal-neutron counting rates fall within the simulation boundaries of possible counting rates consistent with a two-layer model. The fact that most of the data fall above the single layer model suggests that most water-equivalent hydrogen at near-equatorial latitudes is buried below a relatively desiccated layer. This conclusion is reinforced from the correlation between the H_2O abundances derived from fast and epithermal neutrons shown in Figure 11. The solid red line giving the linear regression is seen to have a slope that is less than unity (given by the black line), but

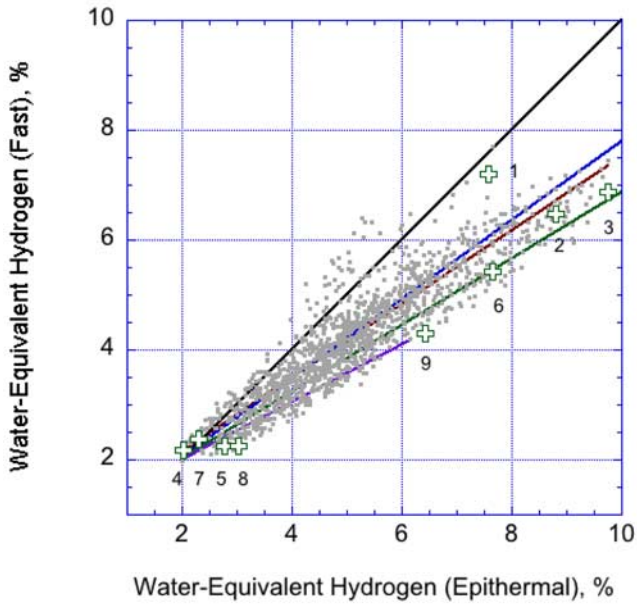

Figure 11. Correlation between water-equivalent hydrogen derived from fast and epithermal neutron counting rates using equation (1). Data points correspond to measured counting rates between ±45° latitudes in quasi equal-area spatial elements each having areas equal to 5° × 5° latitude by longitude squares at the equator. The solid red line gives the linear regression between fast and epithermal water-equivalent hydrogen estimates given by M_{H2O}(Fast) = 0.67 M_{H2O}(Epi) + 0.008, with a correlation coefficient of R = 0.92. The solid black line gives M_{H2O}(Fast) = M_{H2O}(Epi); the blue, green, and purple lines give model results for 10, 20, and 40 g/cm^2 of soil containing 2% H_2O. The numbered crosses give the selected near-equatorial sites listed in Table 3.

closely equal to that predicted for a 10 g/cm^2 thick layer of 2% H_2O that overlies a semi-infinite H_2O-bearing layer (blue line from Figure 8). Also shown in green and purple are the regressions predicted for overlying 20 and 40 g/cm^2 thick layers from Figure 8.

[32] The good agreement between the blue and red lines in Figure 11 then favors the model of equatorial and mid latitudes shown in Figure 2, in which a semi-infinite layer containing X% H_2O is buried beneath a 2% H_2O layer having an average thickness of about 10 g/cm^2. However, this thickness may vary from place to place because, while measured epithermal neutrons are not sensitive to composition, measurements of fast neutron currents from the Moon revealed variability at the ±15% FWFM level [*Feldman et al.*, 1998; *Maurice et al.*, 2000; *Gasnault et al.*, 2001]. Indeed, the vertical widths of H_2O from fast neutrons in Figure 11 amounts to about 30% FWFM at mid range.

[33] The regression line for a 10 g/cm^2 2% H_2O layer shown in Figure 8 can be used to convert the map of H_2O generated from measured epithermal neutron currents to one for the mass fraction of H_2O in the lower semi-infinite water-bearing layer. The relation between actual and apparent H_2O mass fractions (see Figure 7) can be fit quite well (having a correlation coefficient of R = 0.996) by the polynomial

$$M_{H2O}(\text{Actual}) = 4.3510^{-4} + 0.998\ M_{H2O}(\text{Apparent}) + 1.784\ M^2_{H2O}(\text{Apparent}). \quad (3)$$

6. Data Summary

[34] About one year of Mars Odyssey NS epithermal and fast neutron data have been used to construct CO_2 frost-free maps of Mars. These data provided input for a map of water-equivalent hydrogen concentrations within about one meter of the Martian surface. Three major reservoirs (other than the minimal atmospheric reservoir) are readily delineated. The two reservoirs that surround the poles extending down to about ±50° latitude have relatively rich deposits of water-equivalent hydrogen. Lower limits of H_2O mass fractions range between 20% and 100%. The third is an equatorial/mid latitude reservoir that is maximized at two locations near the equator. These locations are approximately antipodal and bisect the 0-km elevation contour. H_2O mass fractions in this reservoir range between 2% and 10%, with an average of about 5%.

[35] The north and south high-latitude reservoirs of hydrogen are presented in Figures 5 and 6, respectively. Outstanding features are the residual caps that appear to contain up to about 100% H_2O in the north, and lower values of apparent H_2O in the south. These data are consistent with previous inferences that the residual north polar cap is nearly pure water ice near its surface [*Kieffer et al.*, 1976], and water ice covered by a relatively thin veneer (but thick with regard to neutron transport) of CO_2 ice in the south [*Kieffer*, 1979]. Contours of H_2O mass fractions are superimposed on the MOLA topography poleward of +50° and −50° latitudes in the lower panels of Figures 5 and 6, respectively. Inspection reveals resolved relative maxima in both hemispheres. The maximum in the north is centered on about +70° latitude and −125° longitude, and that in the south is centered on about −70° latitude and 100° longitude. Both maxima are close to a lower-limit abundance of 45% H_2O by mass. These maxima presently have no correspondence with any special surface feature that has been identified. However, the longitudes of pinched-off contours in the lower panel of Figure 5 occur within the deepest portion of the Vastitas Borealis formation near the mouth of chasma borealis. In addition, a relative minimum in H_2O abundance is centered on Olympia Planitia at about 79° latitude and −175° longitude.

7. Discussion

[36] As mentioned previously, a realistic appraisal of the hydrogen content of the top-most layer of the Martian surface from measured fluxes of epithermal and fast neutrons requires knowledge of the stratigraphy of hydrogen-bearing layers. A unique determination of stratigraphy from neutron data, in turn, requires knowledge of the elemental composition of these layers. We start first with a discussion of stratigraphy.

7.1. Stratigraphy

[37] Any attempt to determine the stratigraphy of equatorial/midlatitude hydrogen concentrations faces two obstacles. In principle, the most sensitive measure of hydrogen stratigraphy is provided by correlated variations in thermal and epithermal neutrons. However, application of this technique in practice requires knowledge of the composition of the major thermal-neutron absorbing elements, Fe, Ti, Cl, Gd, and Sm [*Feldman et al.*, 2000]. This composition is not presently available from Mars Odyssey gamma-ray observations. Nevertheless, the measured correlation between fast and epithermal counting rates equatorward of ±45° seems to be consistent with hydrogen-bearing deposits that are buried on average, by about 10 g/cm^2 of soil containing 2% H_2O by mass.

7.2. H_2O Mass Fractions at Selected Equatorial/Midlatitude Sites

[38] Lower-limit estimates of the H_2O abundance for nine selected near-equatorial latitude sites are collected in Table 3. These sites are identified separately by number in Figures 10 and 11. Only three of these sites can be compared individually with estimates made previously, those at the three landing sites. It is important to bear in mind that the exploration scale of the Viking and Pathfinder landing sites (a few meters) is dwarfed by the large neutron footprint of Mars Odyssey (∼600 km), thereby limiting any direct correlation between observed abundances. Initial estimates of the H_2O content of two soil samples at Viking 1 were between 0.1 and 1% mass fraction, and those for two samples at Viking 2 were between 0.8 and 1.0% [*Biemann et al.*, 1977]. A later reanalysis of these data using the engineering model of the Viking Gas Chromatograph Mass Spectrometer (GCMS) in the laboratory on Earth yielded 1.1% and 3.0% for the two samples at Viking 1, and 1.6% and 1.9% at Viking 2 [*Anderson and Tice*, 1979]. The average at Viking 1, 2.1%, is close to our estimate from Mars Odyssey NS data, 3.0 ± 0.4% (3.2% ± 0.4% using the 10 g/cm^2 stratigraphy model given in the

Table 3. Lower-Bound Water-Equivalent Hydrogen Abundances for Selected Sites (5° × 5° Areas)

		Mass Percent of H_2O	
Site	Latitude, Longitude	Semi-infinite	Below 10 g/cm^2 2% H_2O
1) Alba Patera	+40°, −110°	7.6 ± 1.0%	
2) Arabia	−5°, +25°	9.8 ± 1.5%	11.5 ± 1.7%
3) Arabia Antipode	−15°, −175°	8.8 ± 1.3%	10.2 ± 1.5%
4) Argyre	−45°, −45°	2.0 ± 0.3%	2.1 ± 0.3%
5) Pathfinder	+19.3°, −33.6°	2.8 ± 0.4%	3.0 ± 0.4%
6) Sinus Meridiani	0.0°, 0.0°	7.7 ± 1.2%	8.8 ± 1.3%
7) Solis Planum	−25°, −95°	2.3 ± 0.3%	2.4 ± 0.4%
8) Viking 1	+22.3°, −48.2°	3.0 ± 0.4%	3.2 ± 0.4%
9) Viking 2	+47.7°, +134.1°	6.4 ± 1.0%	7.2 ± 1.1%

rightmost column in Table 3), but that at Viking 2, 1.8%, is much less than our estimate of 6.4 ± 1.0% (7.2% ± 1.1% using the 10 g/cm^2 stratigraphy model). Finally, a recent analysis of Alpha, Proton, and X-Ray Spectrometer (APXS) data from Mars Pathfinder used stoichiometry arguments to estimate H_2O abundances from observed excess oxygen, yielded an average H_2O mass fraction for soils ranging up to 1.7% (but generally desiccated), and for rocks ranging between 0.1 ± 1.3% and 4.3 ± 1.3% [*Foley et al.*, 2003]. The high end of the rock estimate is in the range of our estimates of 2.8 ± 0.4% (3.0 ± 0.4% using the 10 g/cm^2 stratigraphy model), while the soil values are mostly lower than our estimates.

[39] Analysis of near infrared spectra measured from above the terrestrial atmosphere [*Houck et al.*, 1973] yielded an average H_2O abundance of Martian soils that amounts to 1% by mass, within a factor of three. Further, their analysis showed that the soil grains that carried this water had a mean particle radius that ranged from 10 to 300 μ (clay-size to fine silt). Fines at the very surface likely dominate the infrared spectra; it is unlikely that duricrusts under the surface dust or anything deeper can be seen by this method. This analysis is supported by a later analysis of data measured using the Imaging Spectrometer aboard the Phobos 2 spacecraft [*Yen et al.*, 1998], which yielded a maximum H_2O abundance of 4% by mass. We note that both of these "global" upper-limit estimates are close to, but slightly less than our midlatitude average lower estimate of 5%.

[40] While the measured H_2O abundances of surface samples in the vicinity of Viking 1 and Pathfinder are in range of those estimated from epithermal neutron data, the surface-sample and orbital estimates at Viking 2 are clearly out of range. Assumption of a different elemental composition cannot account for the difference because our estimate of 6.4 ± 1.0% (7.2% ± 1.1% using the 10 g/cm^2 stratigraphy model), is clearly larger than the surface estimate of 1.8%. A likely resolution of this difference can be inferred from the map in Figure 4. Here, it can be seen that Viking 2 (at +47.7° latitude, +134.1° longitude) lies at the southern margin of the north-polar water-rich terrain, inferred to be buried beneath a relatively hydrogen poor cover, as is inferred from the position of the Viking 2 sample (the data point labeled #9) in Figures 10 and 11. However, we also note that the Odyssey neutron footprint centered over the Viking 2 site includes the water-rich terrain to the north. The high average value of 6.4% water at this site is likely a composite of very water-rich soil to the north with drier soil near and south of Viking 2.

[41] The foregoing rough "validations" of our estimates of H_2O mass fractions have important ramifications for the nature of the equatorial/midlatitude deposits. Our best estimate of a lower limit to the H_2O abundance within these deposits is between 2% and 10%. The largest concentration in this latitude range is high, considering the fact that water ice should not be stable at any depth at latitudes equatorward of ±30° at the present time [*Farmer and Doms*, 1979; *Paige*, 1992; *Jakosky and Haberle*, 1992; *Mellon and Jakosky*, 1993]. One possible explanation is that these deposits contain hydrated minerals [*Feldman et al.*, 2002b; *Bish et al.*, 2003a], possibly in the form of clays, zeolites, hydrous sulfates, hydrous carbonates, hydrous chlorides, and/or other more complex hydrous salts. The role of hydrous minerals could be significant, since they may sequester water as structural H_2O and OH in amounts of ∼10–20% (hydrous silicates), and up to ∼50% (salt hydrates). However, most of these minerals, and the salt hydrates in particular, are unlikely to be stable or fully hydrated at Mars surface conditions. Although some combination of hydrous silicate minerals and salt hydrates may account for some of the observed hydrogen near the equator, their stability in the shallow Martian regolith needs to be determined [*Bish et al.*, 2003b].

7.3. Equivalent Global Thickness of Water

[42] A minimum thickness of a global-equivalent layer, GEL, of water can be estimated from the lower-limit water maps in Figures 4, 5, and 6. This estimate, T(Global), was calculated by integrating zonal averages of the H_2O mass fraction, M_{H2O},

$$T(\text{Global}) = \rho\, D \iint M_{H2O}\, d\Omega/4\pi, \qquad (4)$$

over three contiguous latitude bands, $\lambda > +45°$, $-45° < \lambda < +45°$, and $\lambda < -45°$. Here, T(Global) is the equivalent thickness of H_2O assuming that it is distributed uniformly over the entire Martian surface, ρ is the density of soils near the surface, here chosen to be 1.65 g cm^{-3}, and D is an assumed thickness of the water-equivalent hydrogen deposits. If the thickness of these deposits is D = 1 m, the sensitivity thickness limit for remote neutron observations, then the total inventory of near surface H_2O calculated as full-planet contributions from each zone, amounts to: 4.1 cm for latitudes south of −45°, 5.6 cm for latitudes between −45° and +45°, and 4.4 cm for latitudes north of +45°. Altogether, these estimates yield about a 14 cm GEL of water. Although orbital neutron data can only detect

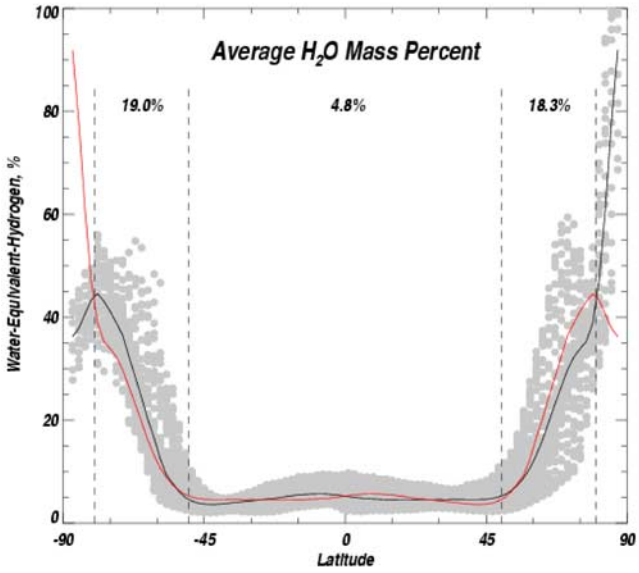

Figure 12. Zonal averages (given by the solid black line) of water-equivalent hydrogen derived from measured epithermal neutron counting rates in quasi equal-area spatial elements equal to the areas of $2^\circ \times 2^\circ$ squares at the equator (given by the gray data points). The solid red line is an equatorial flip of the black line.

hydrogen concentrations within about 1 m of the Martian surface, these deposits could be thicker, and therefore the total water inventory of the observed deposits could be significantly larger.

[43] Another interesting feature of the high-latitude H_2O deposits is illustrated in Figure 12. Here, zonal averages of H_2O calculated from quasi-equal area data (equivalent to $5^\circ \times 5^\circ$ areas at the equator), are plotted by a black solid line that overlays lower-limit H_2O fractions for all equal-area samples. The red line gives the zonal averages with the sign of latitude reversed. This presentation reveals several aspects of the data alluded to earlier. First, there is a sharp break at $\pm 50^\circ$ latitude (delineated by two vertical dashed lines) between relatively low hydrogen abundances at near equatorial latitudes, and relatively high abundances at higher latitudes. Second, the relative maximum at about $\pm 70^\circ$ latitude is seen in both the north and south polar terrains as increased dispersions in H_2O abundance. Third, there is a marked difference between H_2O abundances poleward of $\pm 80^\circ$ (delineated by two vertical dashed lines) that is explained by water ice residual caps that are bare near the surface in the north, and covered by a relatively thin veneer of CO_2 ice in the south. And lastly, the average H_2O abundance of high-latitude terrains between $+50^\circ$ and $+80^\circ$ latitudes in the north is nearly equal to that between -80° and -50° latitudes in the south.

[44] Although there appears to be more water ice in the south, our uncertainties are sufficiently large (roughly ±15% relative uncertainty) that they are equal within errors. This result differs from that derived from an analysis of HEND data [*Mitrofanov et al.*, 2003], where more water ice is inferred in the north than in the south. Although we do not know the origin of the surprising latitudinal symmetry derived from the NS data, the large difference in topography between north and south [*Smith et al.*, 1999], the marked differences in the geologic structure, and differences in aqueous history on geologic timescales of the northern and southern high-latitude terrains [*Carr*, 1996], suggests that none of these can be controlling factors in the present zonally averaged disposition of ground ice at high latitudes. Instead, the north-south symmetry in inferred ground ice and its strong latitude dependence suggest that the structure of high-latitude ground ice as seen in neutrons most likely reflects the latitudinal dependence of soil temperature and an equilibrium with the long-term water vapor content of the atmosphere.

[45] **Acknowledgments.** We wish to thank many of the members of the GRS team for their criticisms and suggestions for clarifications at earlier stages of this study, and to the staff at Los Alamos National Laboratory, U. of Arizona, Lockheed-Martin Astronautics, and the Jet Propulsion Laboratory for their strong support of the ongoing operation of the instrument, the flow of data through the system, and the health of the spacecraft. We also wish to thank both referees for thoughtful criticisms and suggestions for improvement of the original manuscript. Partial support of this work was provided by both the DOE (through laboratory directed research and development) and by NASA, and was conducted under the auspices of the DOE and the University of Arizona.

References

Anderson, D. M., and A. R. Tice (1979), The analysis of water in the Martian regolith, *J. Mol. Evol.*, *14*, 33–38.

Baker, V. R. (2001), Water and the Martian landscape, *Nature*, *412*, 228–236.

Bandfield, J. L., V. E. Hamilton, and P. R. Christiansen (2000), A global view of Martian surface composition from MGS-TES, *Science*, *287*, 1626–1630.

Bevington, P. R., and D. K. Robinson (1992), *Data Reduction and Error Analysis for the Physical Sciences*, 328 pp., McGraw-Hill, New York.

Biemann, K., et al. (1977), The search for organic substances and inorganic volatile compounds in the surface of Mars, *J. Geophys. Res.*, *82*, 4641–4648.

Bish, D. L., J. W. Carey, D. T. Vaniman, and S. J. Chipera (2003a), Stability of hydrous minerals on the Martian surface, *Icarus*, *164*, 96–103.

Bish, D. L., D. T. Vaniman, C. Fialips, J. W. Carey, and W. C. Feldman (2003b), Can hydrous minerals account for the observed mid-latitude water on Mars?, paper presented at Sixth International Conference on Mars, Lunar and Planet. Inst., Houston, Tex.

Boynton, W. V., et al. (2002), Distribution of hydrogen in the near surface of Mars: Evidence for subsurface ice deposits, *Science*, *297*, 81–85.

Boynton, W. V., et al. (2004), The Mars Odyssey gamma-ray spectrometer instrument suite, *Space Sci. Rev.*, *110*, 37–83.

Carr, M. H. (1986), Mars: A water-rich planet?, *Icarus*, *68*, 187–216.

Carr, M. H. (1990), D/H on Mars: Effects of floods, volcanism, impacts, and polar processes, *Icarus*, *87*, 210–227.

Carr, M. H. (1996), *Water on Mars*, 229 pp., Oxford Univ. Press, New York.

Farmer, C. B., and P. E. Doms (1979), Global seasonal variation of water vapor on Mars and the implications of permafrost, *J. Geophys. Res.*, *84*, 2881–2888.

Feldman, W. C., W. V. Boynton, B. M. Jakosky, and M. T. Mellon (1993), Redistribution of subsurface neutrons caused by ground ice on Mars, *J. Geophys. Res.*, *98*, 20,855–20,870.

Feldman, W. C., S. Maurice, A. B. Binder, B. L. Barraclough, R. C. Elphic, and D. J. Lawrence (1998), Fluxes of fast and epithermal neutrons from Lunar prospector: Evidence for water ice at the lunar poles, *Science*, *281*, 1496–1500.

Feldman, W. C., D. J. Lawrence, R. C. Elphic, D. T. Vaniman, D. R. Thomsen, B. L. Barraclough, S. Maurice, and A. B. Binder (2000), Chemical information content of lunar thermal and epithermal neutrons, *J. Geophys. Res.*, *105*, 20,347–20,363.

Feldman, W. C., et al. (2002a), Fast neutron flux spectrum aboard Mars Odyssey during cruise, *J. Geophys. Res.*, *107*(A6), 1083, doi:10.1029/2001JA000295.

Feldman, W. C., et al. (2002b), Global distribution of neutrons from Mars: Results from Mars Odyssey, *Science*, *297*, 75–78.

Feldman, W. C., et al. (2003), CO_2 frost cap thickness on Mars during northern winter and spring, *J. Geophys. Res.*, *108*(E9), 5103, doi:10.1029/2003JE002101.

Foley, C. N., T. Economou, and R. N. Clayton (2003), Final chemical results from the Mars Pathfinder alpha proton X-ray spectrometer, *J. Geophys. Res.*, *108*(E12), 8096, doi:10.1029/2002JE002019.

Gasnault, O., W. C. Feldman, S. Maurice, I. Genetay, C. d'Uston, T. H. Prettyman, and K. R. Moore (2001), Composition from fast neutrons: Application to the Moon, *Geophys. Res. Lett.*, *28*, 3797–3800.

Houck, J. R., J. B. Pollack, C. Sagan, D. Schaack, and J. A. Decker Jr. (1973), High altitude infrared spectroscopic evidence for bound water on Mars, *Icarus*, *18*, 470–480.

Jakosky, B. M. (1991), Mars volatile evolution: Evidence from stable isotopes, *Icarus*, *94*, 14–31.

Jakosky, B. M., and C. B. Farmer (1982), The seasonal and global behavior of water vapor in the Mars atmosphere: Complete global results of the Viking Atmospheric Water Detector experiment, *J. Geophys. Res.*, *87*, 2999–3019.

Jakosky, B. M., and R. M. Haberle (1992), The seasonal behavior of water on Mars, in *Mars*, edited by H. H. Kieffer et al., pp. 969–1016, Univ. of Ariz. Press, Tucson.

Jakosky, B. M., and R. J. Phillips (2001), Mars' volatile and climate history, *Nature*, *412*, 237–244.

Kieffer, H. H. (1979), Mars south polar spring and summer temperatures: A residual CO_2 frost, *J. Geophys. Res.*, *84*, 8263–8288.

Kieffer, H. H., S. C. Chase, T. Z. Martin, E. D. Miner, and F. D. Palluconi (1976), Martian north pole summer temperatures: Dirty water ice, *Science*, *194*, 1341–1344.

Leighton, R. B., and B. C. Murray (1966), Behavior of carbon dioxide and other volatiles on Mars, *Science*, *153*, 136–144.

Leshin, L. A. (2000), Insights into Martian water reservoirs from analyses of Martian meteorite QUE94201, *Geophys. Res. Lett.*, *27*, 2017–2020.

Luhman, J. G., R. E. Johnson, and M. H. G. Zhang (1992), Evolutionary impact of sputtering of the Martian atmosphere by O^+ pickup ions, *Geophys. Res. Lett.*, *19*, 2151–2154.

Maurice, S., W. C. Feldman, D. J. Lawrence, R. C. Elphic, O. Gasnault, C. d'Uston, I. Genetay, and P. G. Lucey (2000), High-energy neutrons from the Moon, *J. Geophys. Res.*, *105*, 20,365–20,375.

Mellon, M. T., and B. M. Jakosky (1993), Geographic variations in the thermal and diffusive stability of ground ice on Mars, *J. Geophys. Res.*, *98*, 3345–3364.

Mitrofanov, I., et al. (2002), Maps of subsurface hydrogen from the High Energy Neutron Detector, Mars Odyssey, *Science*, *297*, 78–81.

Mitrofanov, I., et al. (2003), CO_2 snow depth and subsurface water-ice abundance in the northern hemisphere of Mars, *Science*, *300*, 2081–2084.

Owen, T., K. Biemann, D. R. Rushneck, J. E. Biller, D. W. Howarth, and A. L. Lafleur (1977), The composition of the atmosphere at the surface of Mars, *J. Geophys. Res.*, *82*, 4635–4639.

Paige, D. A. (1992), The thermal stability of near-surface ground ice on Mars, *Nature*, *356*, 43–45.

Prettyman, T. H., et al. (2003a), Mid-latitude composition of Mars from thermal and epithermal neutrons, paper presented at Sixth International Conference on Mars, Lunar and Planet. Inst., Houston, Tex.

Prettyman, T. H., W. C. Feldman, W. V. Boynton, G. W. McKinney, D. J. Lawrence, and M. T. Mellon (2003b), Atmospheric corrections for neutrons reveal variations in surface composition in the Tharsis region, *Proc. Lunar Planet. Sci. Conf. 34th*, abstract 1950.

Prettyman, T. H., et al. (2004), Composition and structure of the Martian surface at high southern latitudes from neutron spectroscopy, *J. Geophys. Res.*, *109*, E05001, doi:10.1029/2003JE002139.

Smith, D. E., et al. (1999), The global topography of mars and implications for surface evolution, *Science*, *284*, 1495–1503.

Squyres, S. W. (1989), Water on Mars, *Icarus*, *79*, 229–288.

Tokar, R. L., W. C. Feldman, T. H. Prettyman, K. R. Moore, D. J. Lawrence, R. C. Elphic, M. A. Kreslavsky, J. W. Head III, J. F. Mustard, and W. V. Boynton (2002), Ice concentration and distribution near the south pole of Mars: Synthesis of Odyssey and Global Surveyor analyses, *Geophys. Res. Lett.*, *29*(19), 1904, doi:10.1029/2002GL015691.

Wänke, H., J. Brückner, G. Dreibus, R. Rieder, and I. Ryabchikov (2001), Chemical composition of rocks and soils at the Pathfinder site, *Space Sci. Rev.*, *96*, 317–330.

Yen, A. S., B. C. Murray, and G. R. Rossman (1998), Water content of the Martian soil: Laboratory simulations of reflectance spectra, *J. Geophys. Res.*, *103*, 11,125–11,133.

Yung, Y. L., J.-S. Wen, J. P. Pinto, M. Allen, K. K. Pierce, and S. Paulson (1988), HDO in the Martian atmosphere: Implications for the abundance of crustal water, *Icarus*, *76*, 146–159.

D. L. Bish, R. C. Elphic, W. C. Feldman, H. O. Funsten, D. J. Lawrence, T. H. Prettyman, R. L. Tokar, and D. T. Vaniman, Los Alamos National Laboratory, Mail Stop D466, Los Alamos, NM 87545, USA. (wfeldman@lanl.gov; thp@lanl.gov)

W. V. Boynton, Department of Planetary Sciences, University of Arizona, Space Science Building, Tucson, AZ 85721, USA.

S. Karunatillake and S. W. Squyres, Center for Radiophysics and Space Research, Cornell University, 428 Space Sciences Building, Ithaca, NY 14853, USA.

S. Maurice, Observatoire Midi-Pyrenees, 9 Avenue du Colonel Roche, Toulouse F31400, France.

M. T. Mellon, Laboratory for Atmospheric and Space Physics, University of Colorado, Duane Physics Building, Campus Box 392, Boulder, CO 80309, USA.

A. E. Metzger and J. J. Plaut, Jet Propulsion Laboratory, MS 183-501, 4800 Oak Grove Drive, Pasadena, CA 91109, USA.